Wang *et al. Biochar* (2026) 8:47
https://doi.org/10.1007/s42773-025-00562-z

Biochar

ORIGINAL RESEARCH Open Access

Different adsorption of organic phosphorus on calcium modified biochar: comprehensive insights from molecular levels

Ning Wang[1,2,3†], Liangjie Tang[1†], Xiaohui Zhang[1], Dongtan Yao[1], Xiaolei Sun[4], Alain Mollier[4], Xiaolong Lin[1*] and Xiaoqian Jiang[1*]

Abstract

Organic phosphorus can cause environmental pollution easily through leaching in natural systems. Here, calcium-modified biochar was prepared to adsorb inositol hexaphosphate (IHP), glycerophosphoric acid (GP), D-glucose 6-phosphate (G6P), and adenine nucleoside triphosphate (ATP), and the impacts of their molecular structures were explored via batch experiments, characterizations, and theoretical calculations. The adsorption of ATP occurred mainly through hydrogen bonding and electrostatic interactions, while that of the others took place through chemical precipitation, where calcium-based active sites functioned and maintained the adsorption stability in different environments. Further, the time-of-flight secondary ion mass spectrometry confirmed the roles of P groups and carbon chains through P-related and CN^- signals. With more reactive P groups (P1,3 and P4,6) and lower molecular electrostatic potentials, IHP achieved significantly higher adsorption (292.1 mg P g^{-1}) although its adsorption energy for a single P group was not optimized. As for GP, G6P, and ATP, the surface occupation by carbon chains became visually prominent. The desorption results showed that released OPs ranged from 20% to 80%, and the adsorption via multiple P groups reduced the desorption of IHP and ATP under different conditions. These results highlight the importance of biochar for OPs' utilization, emphasize the necessity of multi-method sets, and elucidate the molecular mechanisms of interactions.

Highlights

- Phosphate groups and carbon chains jointly determined adsorption mechanisms.
- Chemical precipitation dominated the adsorption of IHP, GP and G6P, while hydrogen bonds and electrostatic interactions functioned for ATP.
- Calcium modification enhanced adsorption capacity in different environments.

Keywords Organic phosphorus, Calcium-modified biochar, Phosphate groups, Carbon chains, Adsorption–desorption mechanisms

[†]Ning Wang and Liangjie Tang have contributed equally to this paper and joint first authors.

*Correspondence:
Xiaolong Lin
linxlong6@mail.sysu.edu.cn
Xiaoqian Jiang
jiangxq7@mail.sysu.edu.cn
Full list of author information is available at the end of the article

Springer

Graphical Abstract

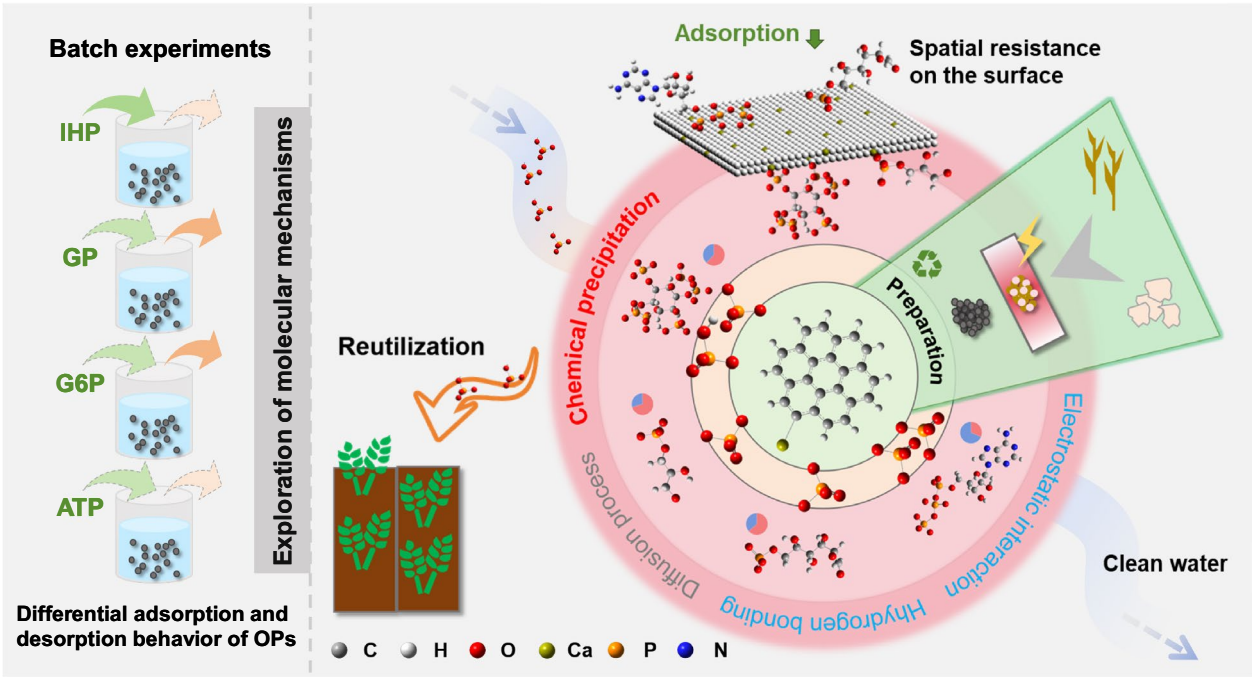

1 Introduction

Phosphorus (P) fertilizers, including the forms of inorganic P (IP) and organic P (OP), have been over-applied to meet production needs, which heightenes environmental risks to adjacent water bodies (Schindler et al. 2016). Ideally, the imported P could remain in soil and continue to mineralize effectively. However, studies have shown that P loss caused by soil erosion and runoff can reach up to 46% of mined P globally (Rittmann et al. 2011). The portion left in soil is firmly adsorbed by minerals or metal ions, further reducing the P supply capacity (Gerke 2015). Hence, controlling P loss while achieving efficient utilization has gradually become a hot topic in green development globally. In this regard, biochar has already stood out among various amendments for its excellent adsorption and release capabilities, and outstanding ecological benefits. Nevertheless, most attempts have been centered on IPs with relatively less attention paid to OPs, although OPs account for 37–73% in fertilizer, and the natural OPs contribute 10–30% of total phosphorus inputs to rivers (Sun et al. 2022). In addition, existing studies focus on comparing adsorption capacities of minerals and modified biochar for IPs and different OPs, while the mechanistic exploration remains superficial, predominantly limited to OPs' molecular weight (MW) and polarity (Yuan et al. 2023; Yan et al. 2014a). This gap poses a significant challenge for fully understanding the prospect of biochar in P management.

Different from IPs, OPs have more complex and diverse forms and structures (Wang et al. 2022). Both P groups and carbon chain structures of OPs may be involved in adsorption–desorption processes. However, there is still a gap in understanding the combined effect of them, as previous studies mainly focused on the roles of P group polarity and MW (Yan et al. 2014a). Therefore, recognizing the actual effects of biochar on OPs is inseparable from our research on different kinds of OPs. According to the literature, we selected four types of OPs to conduct a comparative study, including IHP, GP, G6P, and ATP. These OPs are dominant contributors to enhancing P availability in soil and are deeply involved in the growth of organisms, including the construction of biofilm, transmission of signals, and transfer of energy (Turner et al. 2005). IHP, the main organic P form in soil, has drawn considerable research attention (Gerke 2015). Although the contents of GP, G6P, and ATP are relatively lower than that of IHP, their distinct structural traits may also be linked to their fates in soil (Turner et al. 2005; Manghi et al. 2021). Preliminary studies have shown that the adsorption and leaching of OPs are related to the

soil's P retention capacity and P groups of Ops (McDowell et al. 2021). In soil with high P adsorption capacity, OPs are strongly adsorbed and have low bio-availability. Conversely, the leaching of OPs is significant in soils with low P adsorption capacity, where IHP leached less with multiple P groups and other compounds produced higher leaching rates even than IPs due to insufficient adsorption (Andersson et al. 2013). After leaching, their high bio-availability could cause serious P pollution in waterbodies. Thus, these processes should also be incorporated into the risk assessment and governance of P pollution, while the specific mechanisms by which biochar functions still needs further exploration.

Based on the above understanding, we speculated that these OPs would undergo different adsorption and desorption behaviors with biochar. The rapid development of molecular science and cutting-edge model computing technology has created conditions for us to clarify this speculation at the molecular level. Considering the P adsorption capacity and environmental benefit, this study explored the adsorption mechanism between calcium-modified biochar and OPs. Specifically, calcium modification could introduce calcium-based active sites and regulate surface potential, effectively solving the problems of low adsorption capacity and easy desorption of unmodified biochar. Secondly, calcium-modified biochar utilizes agricultural waste, achieving a green cycle among waste, functional materials and pollutant treatment (Li et al. 2023; Khedulkar et al. 2023). Moreover, calcium-modified biochar exhibits strong selective adsorption for OPs and wide remediation capabilities for soil, such as alleviating soil pH, which renders it highly significant for both risk mitigation and environmental restoration (Singh et al. 2023).

In this study, we chose corn straw and eggshell as raw materials to prepare calcium-modified biochar, studied the adsorption–desorption mechanisms of IHP, GP, G6P and ATP on calcium-modified biochar, and further explored the influence of environmental factors (co-existing ions, ionic strength and pH) on adsorption and desorption behaviors.

The aim was to systematically clarify the intrinsic mechanism between calcium-modified biochar and OP at the molecular level and evaluate its application potential. Our core hypothesis was that active calcium sites of calcium-modified biochar achieved efficient adsorption and stable fixation of OP in complex environments through multiple mechanisms such as hydrogen bonds, electrostatic interaction, and chemical precipitation. The structures of OPs would affect the relative contribution of these mechanisms to adsorption. The results showed that calcium-modified biochar exhibited excellent adsorption capacity within a wide range of OPs concentrations compared to unmodified biochar. The adsorption and desorption process was affected by environmental factors, but remained stable to a certain extent due to the stronger interactions between OPs and calcium-modified biochar. As we emphasized, the molecular morphology of OPs, including P groups and carbon chains, played an important role in the adsorption and desorption processes, leading to the emergence of different adsorption and desorption rates. At the molecular level, these findings deepen our mechanistic understanding of OPs adsorption on calcium-modified biochar. More importantly, these insights could strengthen the scientific basis for optimizing biochar-based technologies in environmental P remediation and sustainable P resource recovery, thereby addressing global P scarcity and water eutrophication challenges.

2 Materials and methods

2.1 Materials and chemicals

The corn straw and eggshell were washed with Milli-Q water, dried at 70 ℃, ground and sieved through a 100-mesh sieve. IHP, GP, G6P, and ATP were purchased from Sigma-Aldrich, Aladdin Chemicals Co., Ltd (Shanghai, China), Acmec Chemicals Co., Ltd (Shanghai, China) and Macklin Chemicals Co., Ltd (Shanghai, China), respectively. All chemical reagents were of analytical grade.

2.2 Preparation of calcium modified biochar

Calcium-modified biochar was synthesized with reference to a previous study (Li et al. 2023). Briefly, 20 g of corn straw and eggshell powder were uniformly mixed at a weight ratio of 1:1 by ball-milling for 24 h, which has been proven to establish the best adsorption performance for phosphate (Yang et al. 2021). The mixture was pyrolyzed at 800 ℃ for 2 h with a heating rate of 5 ℃ min^{-1} under an N_2 atmosphere in the tube furnace (OTF-1200X-5S, HF-Kejing, China), with an N_2 flow rate of 200 mL min^{-1}. Although this pyrolysis temperature (800 ℃) might consume more energy, it was chosen to ensure the complete decomposition of eggshell (mainly $CaCO_3$) and the stable structure of biochar (Cao et al. 2020). After cooling naturally, the eggshell-modified biochar was obtained and washed three times to remove ash, dried at 60 ℃, and ground to a powder evenly. This step was critical for minimizing ash-induced pore blockage upon subsequent use (Huang et al. 2023). The obtained biochar was denoted as CaBC. Unmodified biochar was prepared under the same conditions and named BC.

2.3 Batch adsorption experiments

First, we conducted adsorption experiments on both CaBC and BC to explore the influence of calcium modification. The adsorption kinetics experiments were

conducted in 250 mL bottles by adding 0.05 g of CaBC and 150 mL of solutions of various OPs in triplicate (initial concentration: 350 mg L^{-1}; pH = 7) (Wang et al. 2022; Yan et al. 2014b; Wan et al. 2023), where the high concentration was used to a avoid the occurrence of unsaturated adsorption. The suspension was shaken at 25 ℃ for 24 h, and then filtered through a 0.22 μm PES membrane at different time intervals. In this process, we determined the pH values of the solution after the addition of CaBC and after the adsorption experiment. The adsorption isotherms experiments were carried out by adding 0.01 g of CaBC into 10 mL of solutions with different initial concentrations of OPs (10–400 mg P L^{-1}, pH = 7) in triplicate. The suspension was shaken at 25 ℃ for 24 h, and then filtered through a 0.22 μm PES membrane. After digestion, the P concentration in the filtrate from adsorption kinetics and isotherms experiments was determined by spectrophotometry (Agostinho et al. 2016). Meanwhile, the adsorption experiments of OPs on BC were also carried out under the same experimental setups. Further details on the model equations are provided in S1.

Second, the adsorption capacity of CaBC at a lower OPs concentration was also explored in triplicate. The initial concentration for adsorption kinetics was set at 5 mg L^{-1} (pH = 7), and the initial concentration for isothermal adsorption experiments was set at 1–10 mg P L^{-1} (pH = 7) (Yan et al. 2014b; Wan et al. 2023). This process further demonstrated the adsorption capacity of CaBC for OPs.

Then, to study the effect of coexisting ions and ionic strength, 1 and 10 mM of common anions and cations (Na^+, Ca^{2+}, Cl^-, HCO_3^- and SO_4^{2-}) were separately added to the OPs solution (350 mg L^{-1}; pH = 7). To study the effect of pH, the solution of OPs was adjusted with pH 5–8 (350 mg L^{-1}).

2.4 Desorption experiments

The P-loaded biochar (CaBC-IHP, CaBC-GP, CaBC-G6P, and CaBC-ATP) were filtrated from adsorption experiments. Then, 0.05 g of P-loaded biochar was added into 100 mL of 0.1 M KCl (pH = 7). The suspension was shaken at 25 ℃ for 24 h, and then filtered through a 0.22 μm PES membrane at different time intervals. The concentration of P in the supernatant was measured by spectrophotometry (Agostinho et al. 2016). Further details on the model equations are provided in S2. The effects of environmental factors (co-existing ions, pH and ionic strength) on desorption were studied as follows: 0.1 M KCl at pH 6–8, 0.2 M KCl at pH 7, 0.05 M KCl and 0.05 M $NaHCO_3$ at pH 7.

2.5 Characterization, analytical and computational methods

We uniformly characterized CaBC, CaBC-IHP, CaBC-GP, CaBC-G6P, and CaBC-ATP as follows. The surface area and other pore characteristics of biochar were measured with a surface area analyzer (ASAP 2460) using the Brunauer-Emmett-Teller (BET) nitrogen adsorption method at 77 K. A scanning electron microscope (SEM, EVO MA10) was used to analyze the morphology and surface structure of biochar. The X ray diffraction (XRD, Empyrean), Fourier transform infrared spectrometer (FTIR, NICOLET 6700), X-ray photoelectron spectroscopy (XPS, Thermo Scientific K-Alpha), and zeta potential (Malvern Zetasizer Pro) were conducted to determine the differences in phase composition and functional groups. The time-of-flight secondary ion mass spectrometry (ToF–SIMS) analysis was used to characterize the molecular composition on the surface of CaBC (S3). The solution ^{31}P nuclear magnetic resonance (^{31}P NMR) was used to investigate the adsorption mechanism of IHP on CaBC (S4 and S5). To further visualize the interaction between CaBC and OPs, density functional theory (DFT) calculations were performed on the basis of existing studies (S6) (Yin et al. 2021; Chen et al. 2023; Huang and Hu 2020).

3 Results and discussion

3.1 Characterizations of BC and CaBC

As shown in Fig. S1a, SEM results showed that the surface of CaBC formed a stable carbon fiber structure with rich pores, which might be due to the enrichment of CO_2 produced during the pyrolysis of $CaCO_3$ (Liu et al. 2019). At the same time, resulting calcium-based small particles were uniformly distributed in the pores and on the surface of CaBC (Fig. S1a). Compared with BC, CaBC simultaneously had a decrease in specific surface area and pore volume and an increase in pore size, corresponding to the formation of calcium-based small particles. The differences between BC and CaBC have been described in detail previously (Li et al. 2023). Together, these reactions might increase the adsorption capacity of CaBC. The nitrogen adsorption–desorption curve of CaBC belonged to type "IV" according to the IUPAC classification (Fig. S2a). The H3 type hysteresis loop indicated that CaBC was mesoporous and the shape of mesopores (2–50 nm) was that of slit pores with particle accumulation (Figs. 1a and S2a) (Le Van and Luong Thi 2014). XRD and XPS results showed that the deposited calcium-based active sites were mainly $Ca(OH)_2$ and $CaCO_3$ rather than CaO (Figs. 1b–d and S4c) due to the ease of reaction of CaO from pyrolysis with H_2O and CO_2 (Li et al. 2023).

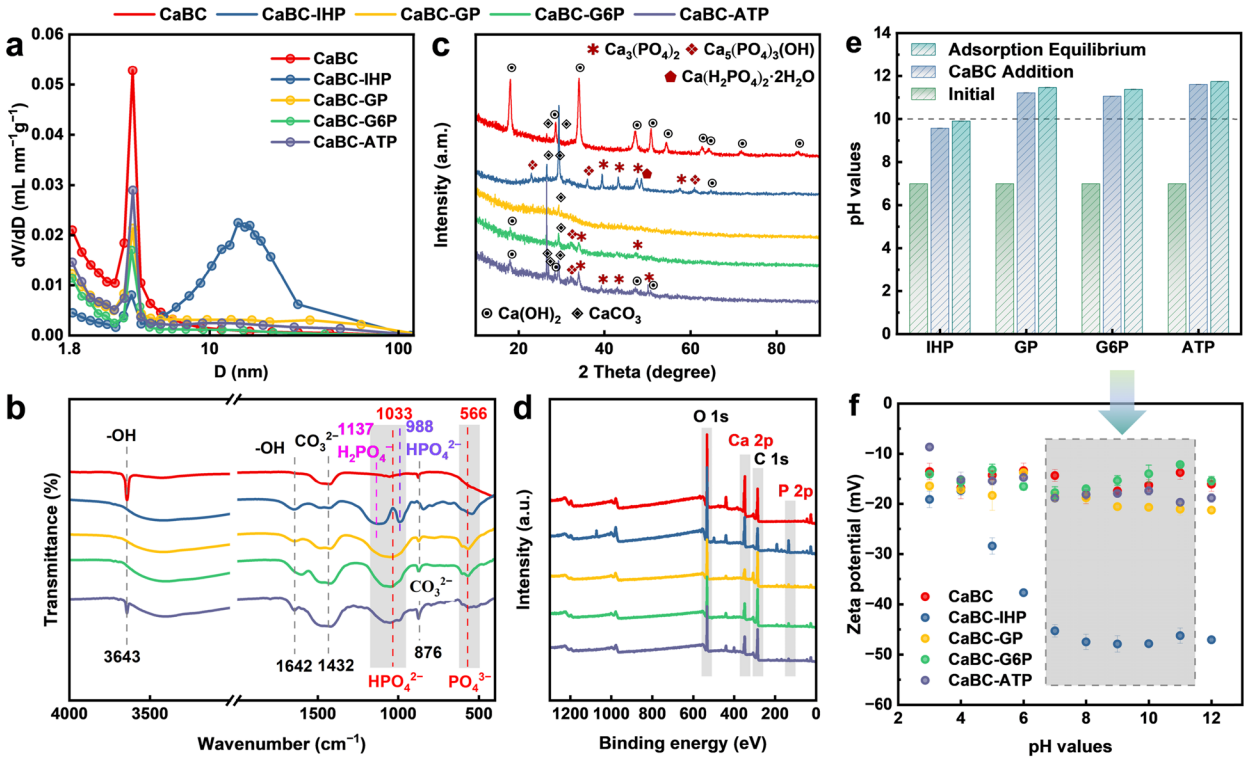

Fig. 1 Pore size distribution (**a**), FTIR (**b**), XRD (**c**), XPS (**d**) analysis of CaBC, CaBC-IHP, CaBC-GP, CaBC-G6P, and CaBC-ATP; the changes of pH values of solution in adsorption kinetics experiments (**e**); zeta potentials of CaBC, CaBC-IHP, CaBC-GP, CaBC-G6P and CaBC-ATP (**f**). All data of pH values and zeta potentials (**e**, **f**) were recorded as the mean and standard error (SE)

The infrared spectrum of CaBC mainly consisted of the vibration of -OH (3643 cm^{-1}), and CO_3^{2-} (1432 cm^{-1} and 876 cm^{-1}), which was in line with the results of CaBC loaded with $Ca(OH)_2$ and $CaCO_3$ (Fig. 1b, c) (Ni and Ratner 2008). Therefore, these results indicated that calcium modification successfully achieved calcium loading on biochar.

3.2 Adsorption performance of OPs on BC and CaBC

The adsorption kinetics of OPs on BC and CaBC are shown in Figs. 2a and S5a–d, and were first investigated with two initial concentrations (5 and 350 mg L^{-1}). The amounts of adsorbed OPs all experienced a rapid initial increase and reached equilibrium within 5 h, where the equilibrium adsorption capacities of BC and CaBC for OPs were both in the following trends: IHP > GP > G6P > ATP, and with the adsorption of IHP being much larger than that of others. Moreover, the adsorption capacity of CaBC for OPs outperformed most reported adsorbents, highlighting its exceptional potential as a functional material for OPs removal. For instance, Yan et al. (2014a, b) employed aluminium oxides as adsorbents for these OPs, where the adsorption capacities were merely 15% of those of CaBC, while the variation in adsorption capacity observed aligns with the findings of this study (Yan et al. 2014a). Moreover, lanthanum-modified biochar, another widely studied adsorbent for P adsorption, only exhibited 50% of the adsorption capacities for IHP and ATP compared to CaBC's performance (Yuan et al. 2023).

The adsorption kinetic results were fitted by pseudo-first-order and pseudo-second-order models and the parameters for both were shown in Table S1, indicating that the adsorption mechanisms were different between adsorbents (BC and CaBC) and OPs (IHP, GP, G6P, and ATP). The adsorption of OPs on BC (initial concentration: 350 mg L^{-1}) and CaBC (initial concentration: 5 mg L^{-1}) showed the same fitting trend where the pseudo-first-order model fitted the adsorption processes of IHP and ATP better ($R_1^2 > R_2^2$, Table S1), but the opposite was true for GP and G6P ($R_1^2 < R_2^2$, Table S1). Additionally, the fitting accuracy of both models was high ($R^2 > 0.95$, Table S1), which suggested that both diffusion and chemical adsorption played important roles (Huang et al. 2014). However, the adsorption of OPs on CaBC (initial concentration: 350 mg L^{-1}) became different in that the adsorption of IHP, G6P and ATP was still controlled by diffusion and chemical adsorption

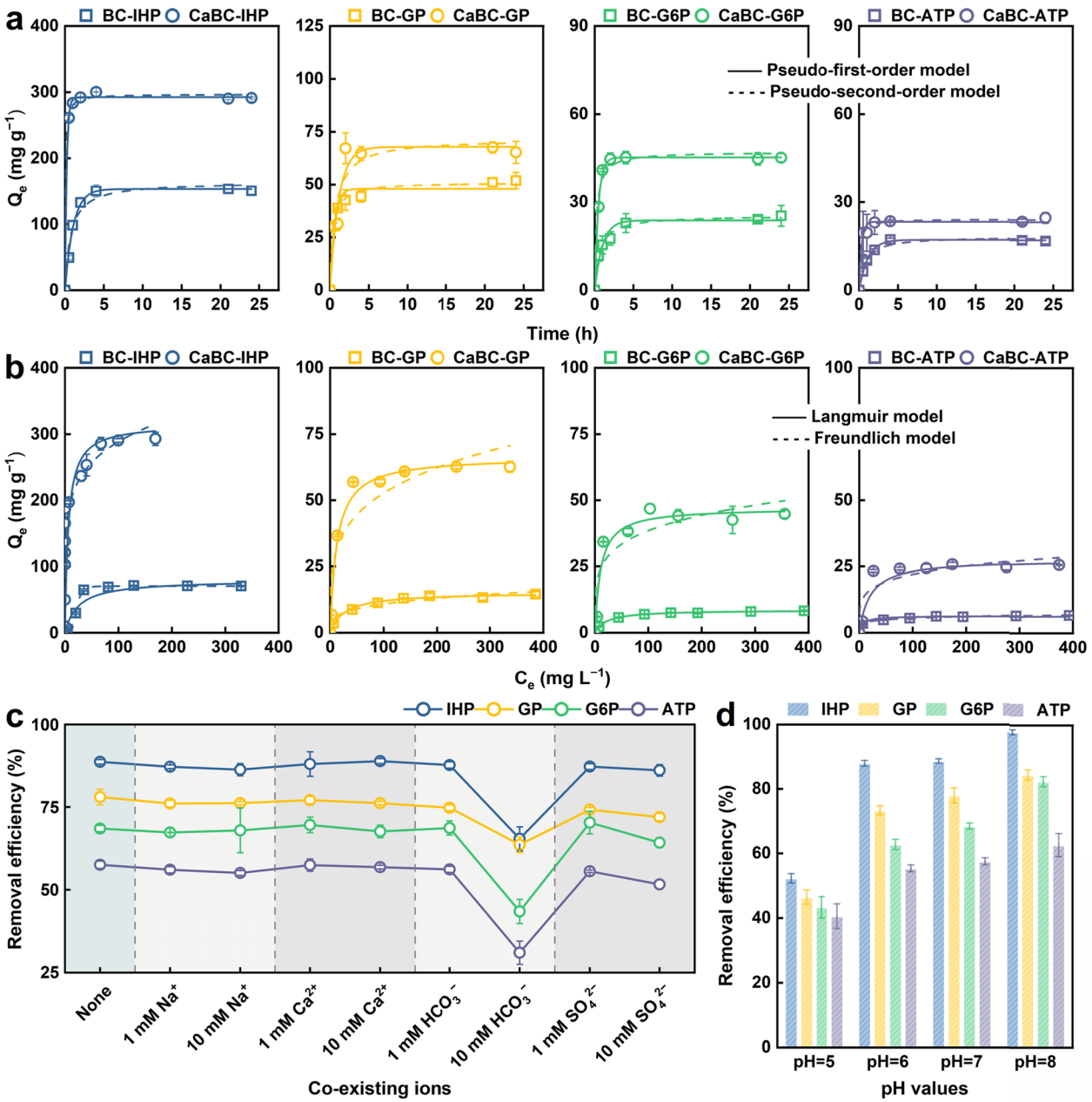

Fig. 2 Adsorption kinetics (**a**) and adsorption isotherm (**b**) models of IHP, GP, G6P, and ATP on BC and CaBC; the effects of coexisting ions and ionic strength (**c**), and pH values (**d**) on adsorption. All data are recorded as the mean and standard error (SE)

processes ($R^2 > 0.95$, Table S1), whereas the adsorption of GP was dominated by diffusion processes ($R_1^2 > R_2^2$, Table S1), possibly related to its smaller relative molecular mass. Consistently, most existing studies suggested that the pseudo-second-order model could better fit the adsorption process of OPs, which might be influenced by pore sizes and site distribution of different adsorption materials (Yuan et al. 2023; Yan et al. 2014a). Furthermore, the increase in initial concentrations of OPs (from 5 to 350 mg L^{-1}) clearly revealed emerging differences in the adsorption capacity of OPs on CaBC (Huang et al. 2014).

The effect of initial OPs concentration on the adsorption capacity of BC and CaBC is shown in Figs. 2b and S5e-h. Increasing concentration led to the expected increase in the adsorption capacity and decrease in the removal efficiency for each OP (1–400 mg L^{-1}, Fig. S5e-h). Further isotherm adsorption models revealed

differential adsorption of OPs on BC and CaBC. For the adsorption of OPs on BC, the Langmuir model fitted IHP adsorption better while the Freundlich model fitted ATP adsorption better, and both models described GP and G6P adsorption well (Table S2). This phenomenon likely stemed from their molecular characteristics: IHP formed a monolayer adsorption with uniform energy via six P groups, ATP created multilayer adsorption through three different P groups, nitrogenous groups, and hydroxyl groups, while GP and G6P produced adsorption with the only P group and hydroxyl groups, enabling multiple outcomes. On the contrary, the Langmuir model better fitted the adsorption of these OPs on CaBC than the Freundlich model (Table S2), where the adsorption all turned into a main monolayer adsorption process with uniform energy and was controlled by the chemical reaction (Koilraj and Sasaki 2017). This transformation highlighted the significant role of calcium modification in the adsorption of OPs. Moreover, we further investigated the effects of environmental factors (coexisting ions and pH) on the adsorption of OPs. As shown in Fig. 2c, the removal of OPs by CaBC with or without coexisting ions still followed the trend: HIP > GP > G6P > ATP, and only the coexistence of 10 mM HCO_3^- significantly decreased the removal efficiency of OPs (IHP:88.71% vs 65.42%, GP:78.04% vs 63.61%, G6P:68.53% vs 43.46%, ATP:57.57% vs 31.04%). Similarly, the increase of pH values maintained the difference in the removal efficiency of CaBC for OPs, but enhanced its removal efficiency (Fig. 2d), aligning with established studies (Chen et al. 2023).

Thus, the results above suggested that CaBC had higher adsorption capacities for OPs than BC, and the adsorption behaviors of different OPs on CaBC were controlled by various mechanisms, which required in-depth research.

3.3 Characterizations of the adsorption processes

The CaBC prepared with eggshell modification had abundant calcium-based active sites (Li et al. 2023), which was consistent with the results that the adsorption of OPs was dominated by a chemical reaction in monolayer (Fig. 1, Tables S1 and S2). Moreover, the adsorption could also occur through the much weaker electrostatic interaction between OPs and other active sites (–OH and –COOH), and through the diffusion process of OPs onto the pore structures (Wu et al. 2021). Therefore, we probed more deeply into the mechanisms of differential adsorption of OPs on CaBC.

After the adsorption of OPs, large Ca–P flocculent precipitation appeared on CaBC (Fig. S1b–e), and the generation of precipitation led to a decrease in the porosity and effective active sites of biochar, corresponding to the significant decrease in specific surface area (S_{BET}) of CaBC after the adsorption of OPs (Table 1). Comparing the adsorption–desorption curves and pore size distribution before and after adsorption (Figs. 1a and S2b–e), we found that the adsorption of OPs increased the pore size of CaBC. Obviously, the micropores (≤ 2 nm) of CaBC decreased after adsorption, while the mesopores (2–50 nm) and macropores (≥ 50 nm) increased (Fig. 1a). In particular, the adsorption of IHP created a more pronounced effect (Fig. S2b). Moreover, the effects of IHP and G6P on the adsorption–desorption curves were different from those of GP and ATP, which was consistent with the fitting results in Sect. 3.2, reflecting the important role of the pore-filling mechanism generated by the diffusion process on the adsorption of IHP and G6P (Fig. S2b–e and Table S1, $R_1^2 > R_2^2$, $R^2 > 0.95$).

Table 1 Surface area and pore structure of biochar samples

Samples	S_{BET} ($m^2\ g^{-1}$)	V_{total} ($cm^3\ g^{-1}$)	D_{BJH} (nm)
CaBC	182.01	0.17	3.83
CaBC-IHP	105.21	0.42	16.01
CaBC-GP	129.45	0.31	9.62
CaBC-G6P	103.74	0.11	4.20
CaBC-ATP	137.05	0.22	6.39

The S_{BET}, V_{total}, and D_{BJH} are BET specific surface area, total pore volume, and Barret-Joyner-Halenda (BJH) adsorption average pore diameter, respectively

XRD and XPS results showed that Ca–P precipitations including $Ca_3(PO_4)_2$, $Ca_5(PO_4)_3(OH)$, and $Ca(H_2PO_4)_2{\cdot}2H_2O$ were generated (Figs. 1c and S4c,d) after adsorption. The occurrence of OPs adsorption was further evidenced by FTIR analysis. After the adsorption of OPs, there was a significant decrease or disappearance of the peak at 3643 cm^{-1}, while new peaks appeared at 566 cm^{-1}, 988 cm^{-1}, 1033 cm^{-1} and 1137 cm^{-1} simultaneously (Fig. 1b), which was attributed to the depletion of –OH and adsorption of Ops (Li et al. 2023). This process may occur not only through Ca–P precipitations formed by the combination of Ca–OH and OPs, but also through electrostatic interaction or hydrogen bonding between –COOH and OPs (Figs. 1c and S4a–c). Of both paths, calcium-based active sites played a crucial role, with more chemical adsorption of IHP and multiple Ca–P precipitations (Li et al. 2023; Wang et al. 2021). Furthermore, the Ca–O remained on CaBC after adsorption could not be neglected based on XPS results, indicating that electrostatic interaction and hydrogen bonding between calcium-based active sites and OPs might have been also instrumental during adsorption (Fig. 1c) (Dai et al. 2020).

It is worth noting that since these OPs all contained hydroxyl structures that could undergo deprotonation, the pH values of solutions would significantly affect their surface charges, resulting in different adsorption

behaviors (Habiba et al. 2022). The results showed that the addition of CaBC remarkably increased the pH values of solutions (Fig. 1e) and promoted the process of deprotonation. Among them, the P groups of GP, G6P, and ATP all underwent complete deprotonation, so the Ca–P formed was mainly $Ca_3(PO_4)_2$ and $Ca_5(PO_4)_3(OH)$ (Fig. 1c and Table S3) (Stockbridge and Wolfenden 2009). For IHP, only three of the six P groups underwent complete deprotonation, consistent with the formation of diverse Ca–P precipitations after adsorption (Table S3) (Torres et al. 2024). Moreover, despite the complete deprotonation of GP G6P, and ATP, the presence of $Ca(H_2PO_4)_2{\cdot}2H_2O$ and HPO_4^{2-} was still observed (Fig. S4c,d), which was related to the hydrogen bonding between Ca–OH and OPs, and consistent with our inference above. Figure 1f shows that whatever the treatment, a negative zeta potential was obtained in the studied pH range and that no isoelectric point was found. In particular, the adsorption of IHP significantly reduced the surface charge of CaBC, which we speculated was because IHP underwent synergistic adsorption through multiple P groups, thereby promoting the adsorption of IHP (Yan et al. 2014a).

Thus, the adsorption between OPs and active sites on CaBC could be expressed by the following reactions (1–5):

$$CaO + H_2O \rightarrow Ca(OH)_2 \quad (1)$$

$$Ca(OH)_2 + H_2O \rightarrow Ca(OH)_2H^+ \quad (2)$$

$$Ca(OH)_2H^+ + PO_4^{3-}/HPO_4^{2-} \rightarrow Ca(OH)_2H^+ \cdots PO_4^{3-}/HPO_4^{2-} \quad (3)$$

$$5Ca(OH)_2 + 3PO_4^{3-} \rightarrow Ca_5(PO_4)_3(OH) \downarrow + 9OH^- \quad (4)$$

$$3Ca(OH)_2 + 2PO_4^{3-} \rightarrow Ca_3(PO_4)_2 \downarrow + 6OH^- \quad (5)$$

The adsorption of OPs on CaBC could be divided into two stages. The initial rapid reaction stage was mainly controlled by ligand exchange, i.e., the substitution of highly active sites on CaBC by OPs, such as –OH groups. In the slow reaction stage, OPs adsorbed on the surface gradually diffused into the interior of CaBC or were converted to various surface precipitations (Fig. 1). Although these adsorption processes could occur for all OPs, the adsorption results among them were vastly different, specifically manifested in the influence on the physical and chemical properties of CaBC, as well as the differences in Ca–P produced by adsorption (Fig. 1). However, based on the characterizations above, we could only recognize the differences in adsorption behaviors and capacities of the OPs on CaBC. t is difficult to identify the molecular basis of such differences, especially what roles their P groups and carbon chains play in this process, respectively.

3.4 Changes in specific signals during adsorption

Compared to traditional analytical tools, ToF–SIMS offers high spatial resolution and surface sensitivity to accurately identify substances based on their mass–charge ratios (m/z) and enables the simultaneous characterization of organic and inorganic components on the surface of materials (Benninghoven 1994; Mei et al. 2022; Huang et al. 2021; Sodhi 2004). Therefore, we further analyzed the interaction of CaBC with OPs through ToF–SIMS, delineating both positively and negatively charged fragments of CaBC before and after OPs adsorption (Figs. 3 and S6).

The intense signals at mass–charge (m/z) ratios of 16, 17, 39, 40, 57, 96, and 113 corresponded to O^-, OH^-, $C_3H_3^+$, Ca^+, $CaOH^+$, Ca_2O^+, and $Ca_2O_2H^+$, respectively (Fig. 3) (Zhao et al. 2024), which confirmed that there were various active sites on CaBC for adsorption. As expected, these peaks were significantly weakened or undetectable after adsorption, and meanwhile, some new signals corresponding to P groups and Ca-P were detected, including PO_2^- (m/z = 63), PO_3^- (m/z = 79), and complex clusters such as Ca_2PO^+ (m/z = 103), $Ca_2PO_3^+$ (m/z = 159), and $Ca_2PO_4^+$ (m/z = 175) (Fig. 3 and Table S4) (Mei et al. 2022). The adsorption of IHP resulted in a greater reduction of these sites compared with other OPs. At the same time, various forms of Ca-P appeared, such as $Ca_3(PO_4)^+$ (m/z = 215), $Ca_3(PO_4)O^+$ (m/z = 231), $Ca_4(PO_4)O_2^+$ (m/z = 287), and $(PO_4)_3O^-$ (m/z = 301) (Fig. S6 and Table S4). Notably, after adsorption onto IHP, the existence of multiple P adsorption was observed (Hilt et al. 2013). Additionally, separate peaks of P groups still existed after adsorption (Fig. 3), suggesting that the adsorption of OPs might occur through the weaker interactions between P groups and –OH of OPs molecules and active sites on CaBC, such as electrostatic attraction and hydrogen bonding. The decrease in O^- and OH^- supported this conclusion (Fig. 3). As a whole, these results were consistent with the characterizations in Sect. 3.3.

Moreover, we detected an obvious peak of CN^- (m/z = 26) on the spectrum of ATP adsorption by CaBC (Fig. 3e), indicating that during adsorption, P groups binded to active sites, while the rest of ATP remained on the surface of CaBC, which might affect the adsorption of ATP (Finšgar 2023). This phenomenon tentatively confirmed our suspicion that the adsorption of OPs on CaBC actually could be affected by their molecular properties, thereby generating differentiated adsorption mechanisms.

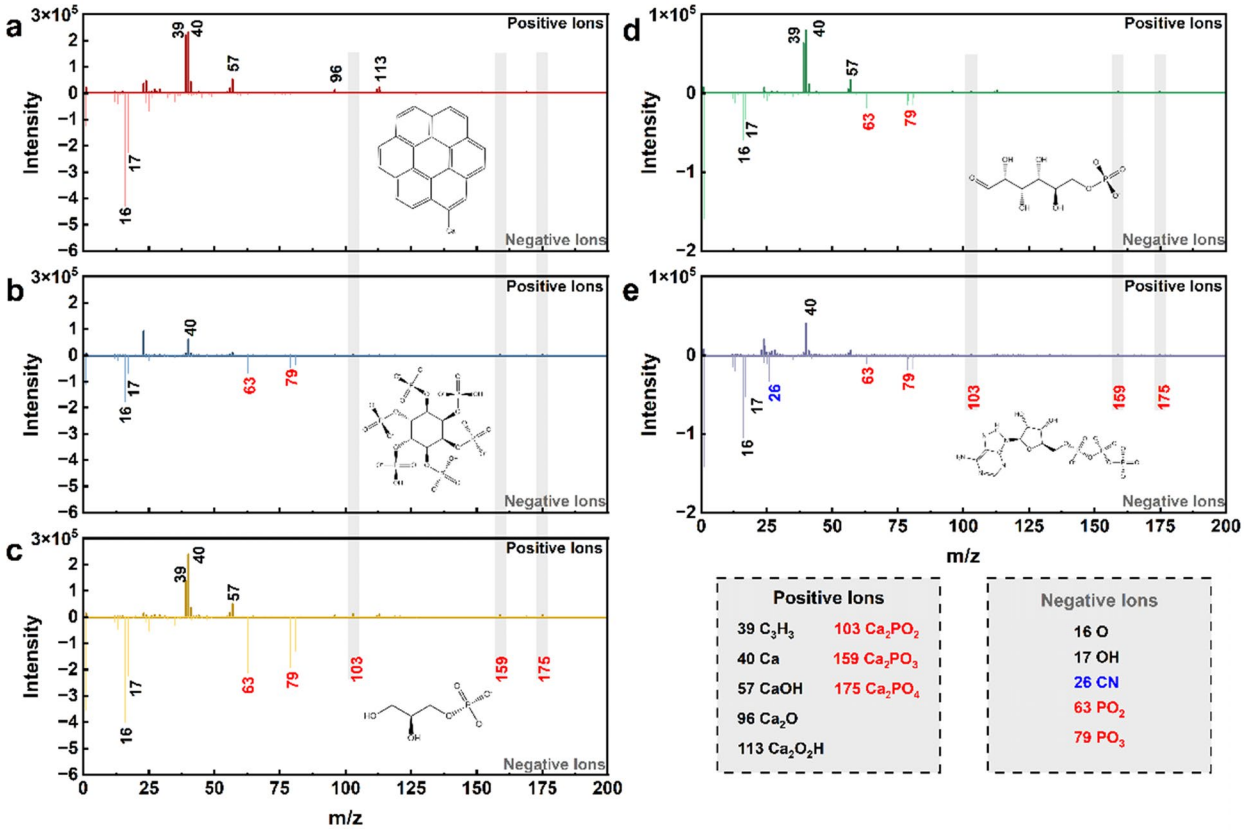

Fig. 3 Characteristic positive-ion and negative-ion fragment patterns of CaBC (**a**), CaBC-IHP (**b**), CaBC-GP (**c**), CaBC-G6P (**d**), and CaBC-ATP (**e**) in the ToF–SIMS spectra for low-masses (m/z: 0–200)

3.5 Determination of preferable P groups of IHP during adsorption

Uniquely, among these four OPs, IHP has multiple P groups that exist independently. When interpreting adsorption behavior, the P groups that participate in adsorption preferentially need to be considered with ^{31}P NMR analysis. Concretely, the changes in chemical shifts of different P groups could give implications of their preferential complexation with CaBC. Normally, the deprotonation of P groups or complex species would cause a downfield shift. However, the coordination with metals, such as the formation of inner-sphere complex, would lead to an upfield shift due to increased shielding around the P nucleus (Xu et al. 2021a).

The positions of peaks of a 5 mM IHP solution were analyzed first before discussing the NMR spectra of CaBC-IHP (Fig. 4a), where the pH value was set at 9.90. From low to high field, the four major peaks were attributed to P5, P2, P1,3, and P4,6 (Tables S5 and S6) (Xu et al. 2021a), which corresponded to the molecular structure of IHP in Fig. S7. The upfield and downfield shifts mentioned below referred to the peak shifts relative to the corresponding peaks in Fig. 4a. In order to explain the contribution of different P groups to complexation, we further observed the ^{31}P NMR spectra of CaBC-IHP at different IHP concentrations to understand the ^{31}P chemical shifts. As shown in Fig. 4b–d, both downfield and upfield shifts peaks were present in P5 and P2, whereas only upfield shifts were present in P1,3 and P4,6, and no peaks were observed like the uncomplexed peaks in Fig. 4a. This indicated that all six P groups of IHP underwent different degrees of inner-sphere complexation with CaBC (Chen et al. 2022). As the initial IHP concentration decreased (from 1.5 to 0.5 mM), the magnitude of the positional changes and the widths of the four peaks increased (Fig. 4b–d), which could be attributed to the deprotonation and complexation of the P groups (Veiga et al. 2014).

In the CaBC suspension with 1.5 mM IHP (Fig. 4b and Table S6), the upfield shifts were observed at P2, P1,3, and P4,6 due to inner-sphere complexation. Downfield shifts were observed at P5, which could be attributed to the deprotonation of P group at P5 (Xu et al. 2021a). In the spectrum of 1 mM IHP-adsorbed CaBC (Fig. 4c and Table S6), more small peaks were observed as a result of inner-sphere complexation and deprotonation. The

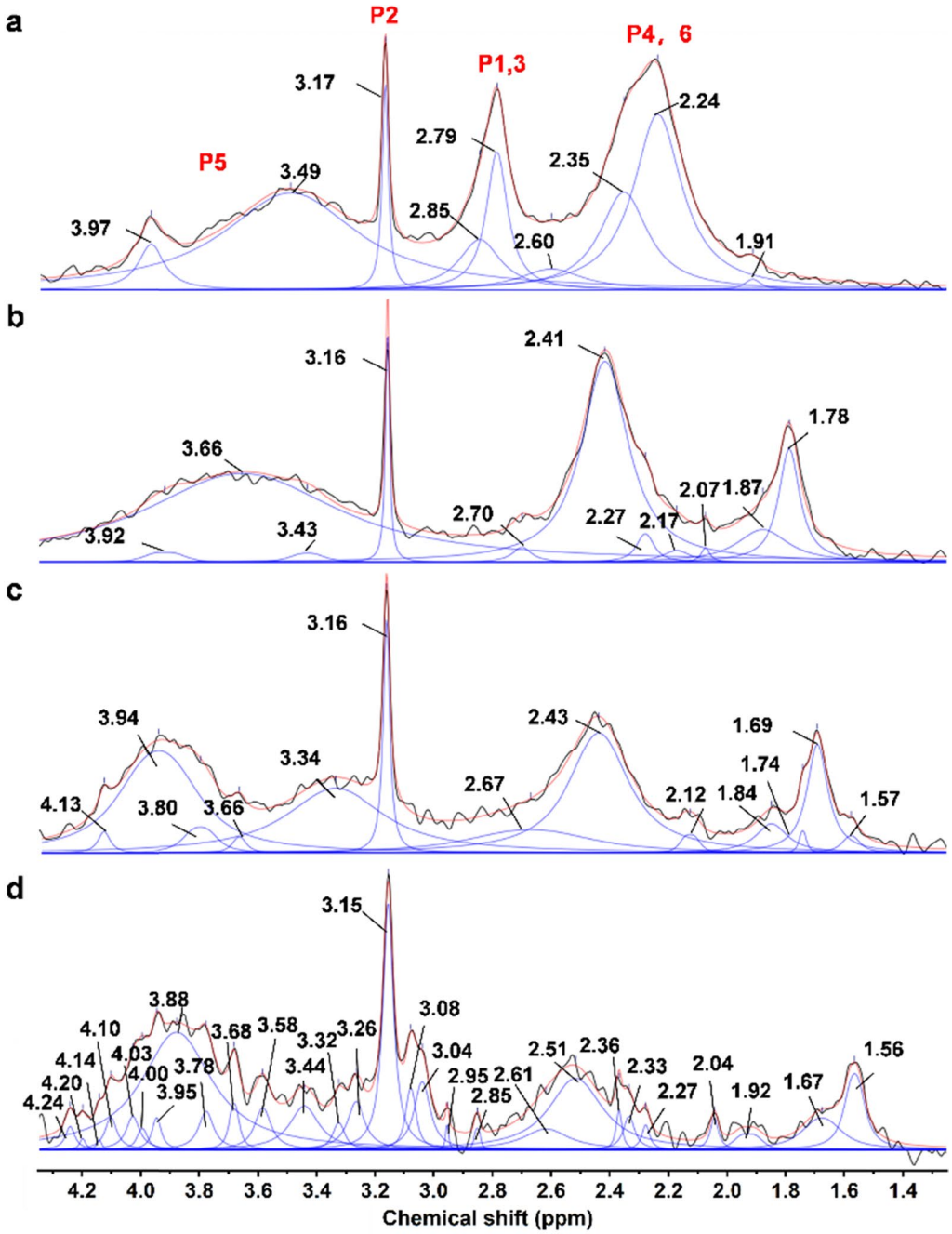

Fig. 4 ^{31}P-NMR spectra: 1.5 mM IHP solution at pH 9.90 (**a**); 1.5 mM (**b**), 1 mM (**c**), and 0.5 mM (**d**) IHP in 0.1 g L^{-1} CaBC suspension at pH 9.90 (**d**). Normalized spectra, deconvoluted peaks, and overall peak fit are shown in black, blue and red, respectively

upfield shifts appeared at P5, P2, P1,3, and P4,6, indicating that these P groups all contributed to inner-sphere complexation. The downfield shifts at P5 were due to the deprotonation of P group and inner-sphere complexation species at P5 (Ren et al. 2019). Similarly, for the spectrum of 0.5 mM IHP-adsorbed CaBC (Fig. 4d and Table S6), the upfield shifts were observed at P5, P2, P1,3, and P4,6, while the downfield shifts were only observed at P2, and P5. These results showed that there were more complex chemical shifts because of inner-sphere complexation and deprotonation, which might be due to the fact that multiple P groups of IHP readily reacted with abundant active sites on the CaBC surface at low IHP concentrations (0.5 mM).

Therefore, synthesizing our knowledge based on ^{31}P NMR results (Fig. 4), P1,3 were the most reactive P groups, followed by P4,6 and P2, while P5 appeared to be the least reactive, which might be related to the conformation of IHP and the different pKa of these P groups. At pH 9.90, complete or partial deprotonation of the six P groups occurred, resulting in the major species of IHP in solution being $[IP_6H_3]^{9-}$ with a small amount of $[IP_6H_2]^{10-}$, and the structure of IHP in the conformations of 1 axial-5 equatorial (1a5e) (Fig. S7 and Table S5) (Xu et al. 2021a). Moreover, these protons were unstable and predicted to form hydrogen bonding within the molecule through an internal rearrangement, influencing the ability of P groups in adsorption (Chen et al. 2022). Specifically, for the three protons of $[IP_6H_3]^{9-}$, the one was strongly shared by P1,3 and P2, and another by P4,6 and P5, while the third proton might preferentially associate with P1,3 and be probably shared between neighbouring P groups (Table S5) (Veiga et al. 2014). Further analyzing the chemical shifts of different P groups, we found that P1,3 and P4,6 mainly formed inner-sphere complexation, while P2 and P5 simultaneously produced inner-sphere complexation and deprotonation during the adsorption (Table S6). It was speculated that the adsorption of P2 and P5 could break their hydrogen bonding with protons, resulting in deprotonation, while this process was weakened by the remaining hydrogen bonding in the adsorption of P1,3 and P4,6, resulting in a lack of downfield shift in the spectra (Fig. 4b–d and Table S6) (Xu et al. 2021a). This effect was also reflected in the preferential adsorption of these P groups that had a stronger and more association with protons; P1,3 would become the best candidates for charge attraction to the negatively charged CaBC surface (Fig. 1f) (Chen and Arai 2019). Moreover, these results also directly indicated that IHP could adsorb onto CaBC through multiple P groups at the same time and achieve much higher adsorption than others (Fig. 2). The identification of the preferential affinity between different P groups of IHP and CaBC was helpful to understand the internal interaction between CaBC and IHP, and also provided a basis for our subsequent calculations.

3.6 Further confirmation of adsorption mechanisms by DFT method

The adsorption behaviors of OPs on CaBC were various and different. Therefore, in order to further explore the interactions between them at the molecular levels, we integrated the results above into DFT calculations. The optimized model structures were chosen considering the effect of solution pH on the deprotonation of OPs (Fig. 1f and Table S3), which are shown in Fig. S9.

We first calculated the molecular electrostatic potentials (MEP) of CaBC and OPs, to interpret the relative orientation of molecules in complex conformation, and determine the adsorption sites of CaBC and Ops (Fan et al. 2022). The results showed the regions of upper and lower potential, as designated by red and blue colors, respectively (Fig. 5a, b). Consistently, the calcium-based active sites altered the original charge distribution of biochar significantly (Hashemzadeh et al. 2024). The difference in electronegativity between calcium and carbon atoms efficiently modulated the charge distribution near the doping position, thus causing charge transfer and producing the largest positive potential in the prominent part of calcium (Fig. 5a) (Ma et al. 2023). Moreover, other regions of CaBC also became generally positive potential, creating conditions for the adsorption of OPs through electrostatic interaction (Fig. 5a). On this basis, we speculated that the differences in MEPs of OPs might have influenced their adsorption behaviors. The results showed that all OPs had the lowest negative potential of molecules at their P groups, which made them easily adsorbed onto the positive potential regions of CaBC (Fig. 5b). In addition, the absolute values of the lowest potential sites of OPs decreased according to the trend of IHP > ATP > GP > G6P (Fig. 5b). Thus, IHP might have a prominent adsorption capacity for CaBC, corresponding to the results of adsorption and zeta potentials (Figs. 1f and 2).

Molecular orbital (MO) theory provides a visual representation for recognizing the reactivity of molecules (Habiba et al. 2022). We calculated the highest occupied molecular orbital (HOMO) and lowest unoccupied molecular orbital (LUMO) of OPs to explore their potential to interact with CaBC (Fig. 5c). The results showed that the energy gaps between HOMO and LUMO exhibited a trend of GP > IHP > ATP > G6P. Generally, the larger the gap is, the more energy is required to transform from LUMO to HOMO is required, and the less reactive the molecule is (Habiba et al. 2022). Therefore, the reactivity of OPs was G6P > ATP > IHP > GP. Further analysis of MO diagrams of OPs indicated that their distributions of HOMO and LUMO were in line with those of the electric charge (Fig. 5b, c). Concretely, HOMO and LUMO were respectively distributed on both sides of the molecular structures, and the HOMO was always occupied by P groups, suggesting that OPs were highly capable of electron transfer and owned strong activity (Liang et al. 2022). In addition, we further analyzed the diagrams of IHP, and found that the LUMO was concentrated at P1/P3 determined by ^{31}P NMR, while the HOMO was mainly distributed at P4,6, and also at P3/P1 (Figs. 5c and S7), which indicated that P groups at P1,3, P4,6 were more active, consistent with the NMR results above.

After determining the adsorption sites of CaBC and OPs, we attached these OPs to the optimal structure of

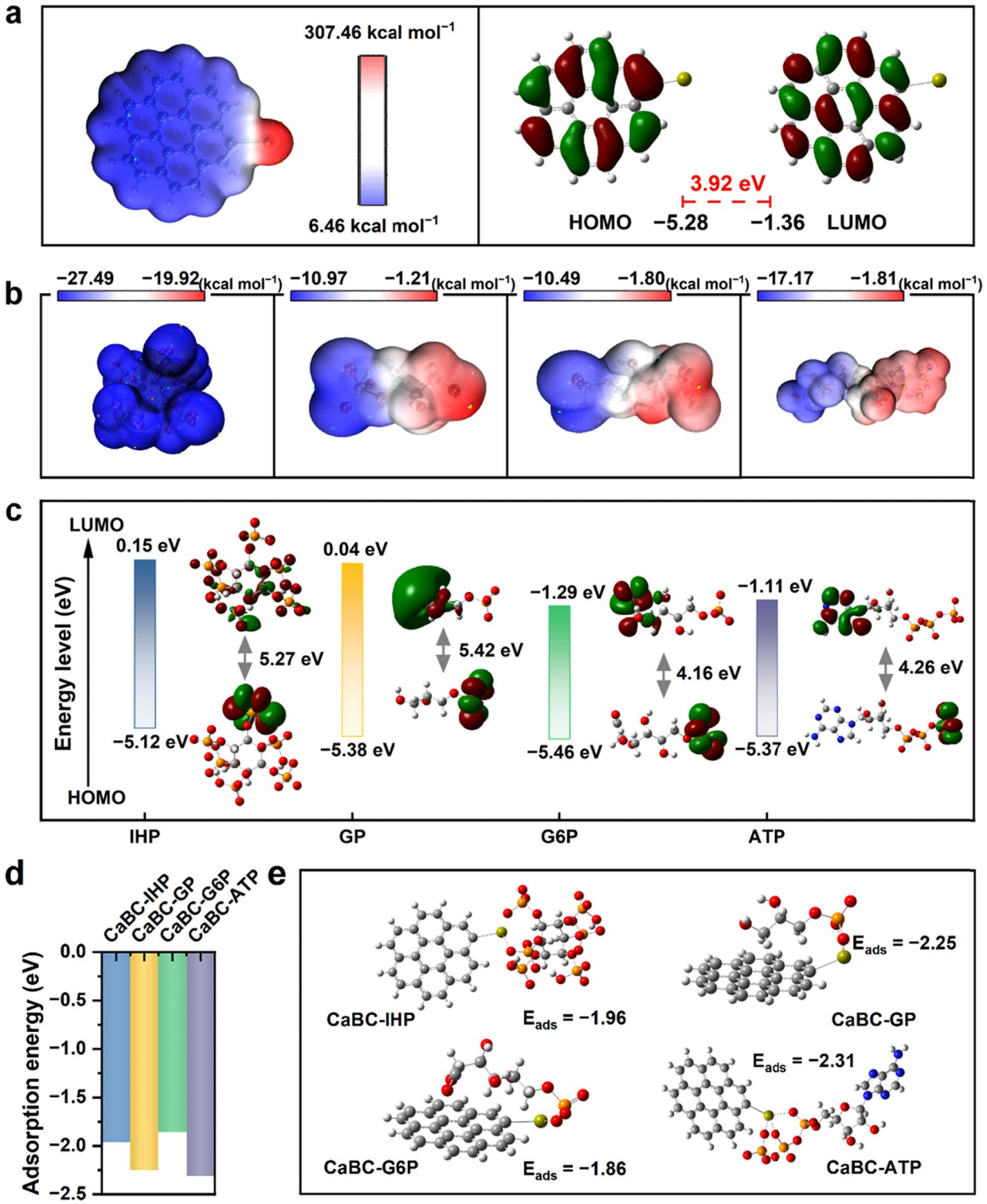

Fig. 5 The molecular electrostatic potentials and HOMO and LUMO energies of CaBC (**a**); the molecular electrostatic potentials (**b**) and HOMO and LUMO energies (**c**) of OPs; structural diagrams of CaBC after adsorption (**e**). The gray, white, red, yellow, orange, and blue spheres represent C, H, O, Ca, P, and N atoms, respectively

CaBC, and the matched structural diagrams and adsorption energy data were shown in Fig. 5d, e. The adsorption energy (E_{ads}) is a fundamental thermodynamic parameter used to quantify the changes in the total energy of the system before and after adsorption, which is considered a key criterion for elucidating the complexity of adsorption mechanism (Yan et al. 2020). The negative values of adsorption energy confirmed that the adsorption reaction was energetically spontaneous (Du et al. 2022). We found that the absolute value of E_{ads} decreased in the order of ATP > GP > IHP > G6P. The higher the absolute value of adsorption energy was, the stronger the adsorption of OPs on CaBC was occurred.

Taken together, the results of DFT calculations were not entirely correspond to the results that the adsorption capacities on CaBC followed the trends: IHP > GP > G6P > ATP, and with the adsorption of IHP being much larger than others. One important reason for this contradiction was that DFT calculation only considered the most stable conformation when a single OP molecule underwent adsorption on CaBC, while the adsorption of OPs on CaBC occurred simultaneously with multiple molecules in batch experiments. Therefore, our understandings of the DFT calculation results needed to be based on the adsorption results of batch adsorption. Specifically, IHP exhibited the highest adsorption despite its poor reactivity and affinity, suggesting that the adsorption of IHP was mainly controlled by its negative charge (Fig. 5b). Besides, with multiple P groups involved in surface coordination (Fig. 4), IHP could form more stable surface complexes (Yan et al. 2014a).

Compared with considering only a single group, synergistic adsorption of multiple P groups was believed to increase the absolute value of E_{ads}, explaining why IHP's high adsorption capacity coexisted with its low E_{ads} for a single P group with CaBC (Huang et al. 2025). The specific quantitative analysis of this process requires future in-depth characterization through competitive adsorption experiments or binding energy calculations. Correspondingly, we found that when the highly reactive P1/P3 was chosen to form adsorption with CaBC based on the NMR results, P2 could also undergo adsorption, producing simultaneous adsorption of multiple P groups at the same calcium active site (Fig. 5e). In order to minimize the cation-cation electrostatic repulsion, the caluim (Ca^{2+}) on CaBC tended to move away as far as possible from the incoming proton (H^+), towards the P1,3-P2 zone and causing the adsorption of P2 (Veiga et al. 2014). During this process, the protons rearranged so that the first proton was associated with P3/P1 and P2, the second could fill the P3/P1-P4,6 zone and the last one would be attached to P5 and P4,6. Moreover, in the conformations of 1 axial-5 equatorial (1a5e) (Fig. S7), it was reasonable to suggest that P4,6 and P5 could be associated with other CaBC, and bridge more CaBC together, which has been also reported by others (Xu et al. 2021a). The particle bridging effect may further promote the adsorption of IHP and increase the stability of CaBC-IHP after adsorption.

Compared to IHP, GP and G6P could only bind to CaBC through one P group. Their carbon chains and glucose moieties were spatially site-blocked from the CaBC surface, attenuating their adsorption although both of them have higher affinity or reactivity than IHP (Fig. 5d, e) (Chen et al. 2021). Additionally, observing the structural diagrams of GP and G6P after adsorption, we could find that their adsorption significantly occupied the surface space of CaBC, which would in turn reduce the subsequent continued adsorption of OPs (Fig. 5e). Theoretically, the affinity of ATP was greater than that of GP and G6P because the adenosine moiety of ATP was farther away from the terminal P group, and thus had less influence on ATP adsorption (Xu et al. 2021b). Moreover, tri-polymerized P groups in ATP could be coordinated to the surface through more hydroxyl groups (Yan et al. 2014a), which was in agreement with the affinity and reactivity between CaBC and ATP (Fig. 5e). However, it was found that the adsorption of ATP was lower than that of GP and G6P, which might be due to the larger relative molecular mass of ATP (505) than that of GP and G6P (172 and 260). The molecular weight of OPs was related to their spatial site resistance effect on the surface of CaBC (Chen et al. 2021). The higher the molecular weights, the higher its spatial site resistance is, and the more difficult the adsorption of OPs is. Therefore, although ATP had a higher affinity with CaBC, its larger molecular weight limited its adsorption behavior on the surface. At the initial stage of adsorption, ATP adsorbed rapidly on CaBC with high affinity. Later, the continuously increasing repulsive force between ATP and the spatial site inhibition between ATP and CaBC made adsorption difficult, which finally masked the intrinsic adsorption affinity advantage of ATP. Consistent with this, although ATP also has multiple P groups and showed a higher affinity with CaBC, its adsorption capacity was much lower than that of IHP (Fig. 2). These results further emphasized the strong restriction on the adsorption by the space occupation of the carbon chains in the ATP molecular structure.

In conclusion, the combination of DFT calculations and characterizations helped us to jointly understand the reasons for the differential adsorption behaviors of CaBC for different OPs. The underlying mechanism governing the adsorption process could be presented with a schematic illustration, with a comprehensive coverage of adsorption phenomena, including chemical precipitation, diffusion

process, hydrogen bonding, and electrostatic interaction (Fig. S10).

We further preliminarily measured the contributions of these mechanisms (Fig. S11), and the results showed that the importance of them varied among OPs. For IHP, GP and G6P, the Ca–P precipitations produced by PO_4^{3-} accounted for considerable proportions of adsorption capacity, reaching 61.93–70.71%, indicating that the chemical precipitation played a dominant role during adsorption, while the contributions of hydrogen bonding and electrostatic attraction were only 29.29–38.07%. While for ATP, hydrogen bonding and electrostatic attraction played more significant roles, reaching 66.51%, consistent with the density functional theory (DFT) calculation results, where P groups in ATP were all attracted by calcium-based active sites. The weak influence of ionic strength indicated that the role of pore diffusion in this process was relatively small (Fig. 2c). The dissection of these mechanisms enhanced our understandings of the adsorption differences among OPs. It is worth noting that due to the structural complexity of OPs, their adsorption on CaBC may proceed stepwise. DFT calculations and non-in-situ characterizations have elaborately revealed the results of the adsorption of OPs on CaBC, but visualizing the process still requires the application of transition state analysis and in-situ characterization in future.

3.7 Mechanism of the effects of co-existing ions and pH on the adsorption of OPs

The coexisting anions and cations including Na^+, Ca^{2+}, Cl^-, SO_4^{2-} had little effect on the adsorption of OPs (Fig. 2c), consistent with the potential for forming inner-sphere complexation by CaBC (Wan et al. 2023). Nevertheless, at high ionic strength (10 mM), the coexisting HCO_3^- reacts with the calcium-based active sites of CaBC through ligand exchange and precipitation formation, markedly reducing the removal efficiency of 14.43–26.53% (Wan et al. 2023; Yin et al. 2024). Furthermore, the weak influences of Cl^- and SO_4^{2-} indicated that ligand exchange of anions played a relatively small role in reducing OPs' adsorption (Zhang et al. 2019). Unlike co-existing ions, the pH of the solution may have a significant impact on both the surface properties of CaBC and the morphology of OPs. However, as the pH increased, the zeta potentials of CaBC only changed slightly (Fig. 1f), but OPs gradually underwent a deprotonation process, leading to an increase in their negative charge (Fan et al. 2022). DFT calculations showed that after modification, localized positive charges appeared in the CaBC, which increased the adsorption of OPs (Fig. 5a). Therefore, the increase in the negative charge of OPs caused by an increase in pH could enhance the electrostatic attraction between OPs and calcium-based active sites, thereby increasing the adsorption of OPs. Furthermore, under these conditions, Ca^{2+} was also easily adsorbed by OH^- in the solution, generating more Ca-OH as the increase in pH, and thus promoting the adsorption of OPs through electrostatic attraction and hydrogen bonding, etc. (Li et al. 2023). This process might also explain why the adsorption of OPs (GP, G6P, and ATP) was still affected by an increase in pH after complete deprotonation (Table S3). Overall, environmental conditions directly or indirectly affected the adsorption behaviors of CaBC for OPs. However, calcium active sites had high stability and could maintain the removal ability of CaBC for OPs under different conditions, which has been proven to have great potential for P pollution control.

3.8 Evaluation of desorption capacity of CaBC-OPs

Understanding the desorption capacities of OPs after adsorption could better evaluate the role of CaBC in the rational utilization of resources. The desorption of OPs was rapid within 0.5 h, after which it gradually reached equilibrium (Fig. S12). The rapid desorption at the beginning might be due to the equilibrium shift of OPs adsorbed on CaBC between the solid-phase surface and initial phosphorus-free solution, leading to desorption of OPs from the CaBC surface. Besides, the Cl^- in solution could also undergo ion exchange with OPs. And as the concentration of OPs increased, their release became more difficult, until an adsorption–desorption equilibrium was achieved (Ruttenberg and Sulak 2011).

In addition to the same changing trends, we found that the OPs desorption capacity of CaBC varied. Specifically, the OPs desorption rates of CaBC-GP and CaBC-G6P were significantly higher than those of CaBC-IHP and CaBC-ATP (Fig. 6a and Table S7), similar to the results of an existing study (Yan et al. 2014a). Combined with the characterization of CaBC adsorption of OPs above, the differences might be related to the strength of adsorption that OPs formed with CaBC. We calculated HOMO and LUMO before and after the adsorption of OPs on CaBC to gain insights into the desorption differences (Figs. 5a and 6b). After adsorption, the energy gaps of complexes were reduced compared to those of OPs and CaBC, which was inconsistent with the results of phosphate adsorption on calcium-modified biochar, indicating that the adsorption of OPs created pronounced effects on the stability of CaBC structure due to their larger molecular weights (Yin et al. 2021).

Among these OPs, the energy gaps between HOMO and LUMO showed a trend of CaBC-G6P > CaBC-GP > CaBC-IHP > CaBC-ATP (Fig. 6b). Therefore, after adsorption, the reactivity showed a trend of CaBC-ATP > CaBC-IHP > CaBC-GP > CaBC-G6P. Further

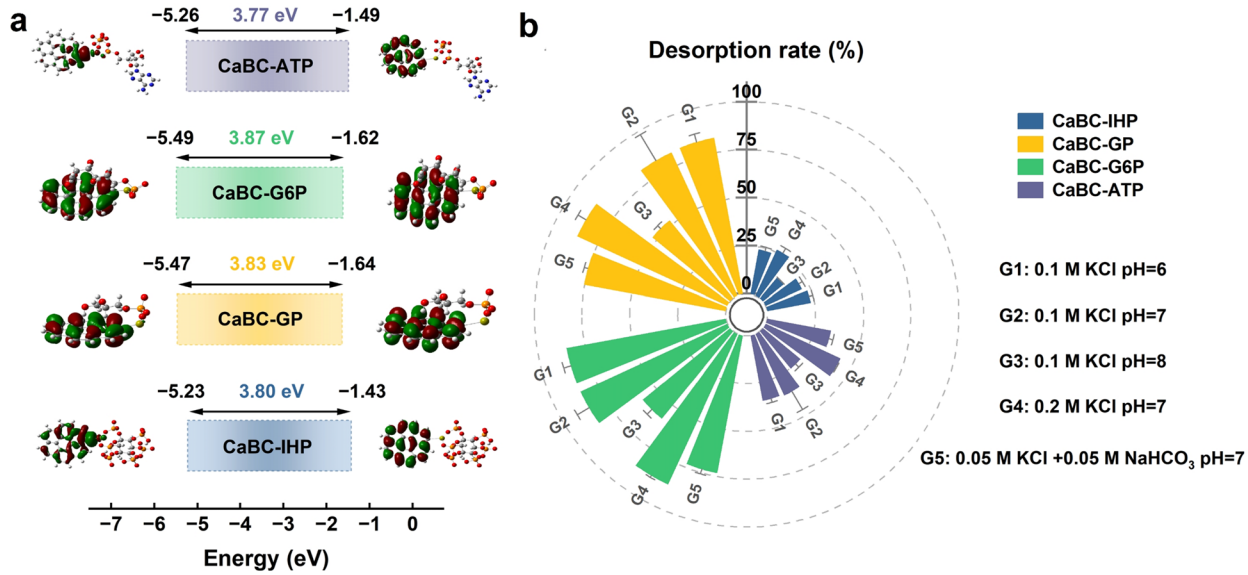

Fig. 6 HOMO and LUMO energies of CaBC after adsorption (**a**); the effects of coexisting ions, ionic strength, and pH values on desorption (**b**). The gray, white, red, yellow, orange, and blue spheres represent C, H, O, Ca, P, and N atoms, respectively

analysis of diagrams revealed that the HOMO and LUMO distributions of CaBC-GP and CaBC-G6P were mainly in the CaBC fraction, whereas those of CaBC-ATP and CaBC-IHP showed some variations between CaBC and OPs, accompanied by electron transfer in this process, indicating that CaBC-ATP and CaBC-IHP should have high activity and poor structural stability (Liang et al. 2022). However, as we have also mentioned above, multiple P groups of IHP could be adsorbed to form more stable surface complexes (Fig. 1c). Therefore, when we only considered the involvement of a single P group in the adsorption of CaBC-IHP, the complexes formed might have poorer stability. The poorer stability but lower desorption rate of CaBC-ATP may be related to the lower adsorption amount of ATP, in which the repulsive force between ATP inside CaBC-ATP was less and the adsorbed ATP was more difficult to desorb (Fig. 2). Thus, in addition to the inherent adsorption differences caused by the molecular structures of OPs, the actual adsorption conditions of OPs on CaBC could also affect their desorption behaviors.

Moreover, further analysis revealed that the desorption behavior of OPs was influenced by environmental factors. The decrease in desorption rate caused by the increased pH (from 6 to 8) might be related to the increased affinity between CaBC and OPs, aligning with the pH-dependent removal efficiency trends of OPs by CaBC (Figs. 2c and 6c), which together confirm pH's consistent roles in both adsorption and desorption. Under the same pH conditions, the increase in ionic strength promoted the desorption of OPs, while the presence of HCO_3^- reduced it (Fig. 6c). An increase in the concentration of Cl^- would compress the thickness of double electric layer on CaBC surface and weaken the effective distance of electrostatic attraction between CaBC and OPs. These factors enhanced the ability of Cl^- to compete for active sites with OPs, further leading to the occurrence of ligand reaction (Tofan-Lazar and Al-Abadleh 2012). Compared with Cl^-, the lower charge density and larger hydration radius of HCO_3^- result in a slower migration rate in the diffusion layer, and the dynamic equilibrium of its protonation may reduce the effective competitive concentration, showing a competitive adsorption disadvantage compared to Cl^- (Zhang et al. 2019). Therefore, understanding these differences could be crucial for the rational selection of adsorption materials and the optimization of water treatment processes.

3.9 Potential application of CaBC as a P synergistic material

Biochar is a highly stable adsorption material produced by pyrolysis, which could last for a long time in soil and water. However, the adsorption and desorption behaviors of OPs on biochar have been overlooked previously for efficient P management. In this study, CaBC with eggshell and corn straw as raw materials was prepared, which could effectively adsorb various OPs, including IHP, GP, G6P, and ATP, and be reused as a slow-release fertilizer. Based on the results of this and previous studies, calcium-modified biochar showed good adsorption

and release effects of various P components, including IPs and OPs, which may have great potential in improving the efficient utilization of P. Moreover, both raw materials used for calcium-modified biochar were wastes in agricultural production and daily life. When we conducted a life cycle evaluation of CaBC to understand its ecological benefits, the environmental impact of the preparation process would be minimized, which had a significant advantage in realizing green management compared to the modification with purified reagents such as $CaCl_2$ (Chen et al. 2024).

Overall, CaBC has demonstrated high adsorption capacity for P and outstanding anti-interference ability, and has breakthrough value in areas such as targeted environmental remediation, long-term phosphate fixation, and precise functional material design. Phosphorus in agricultural non-point source pollution and industrial wastewater has strong mobility. CaBC effectively achieves selective capture and long-term fixation of phosphorus through chemical fixation and physical interception, reducing phosphorus environmental pollution. The phosphorus adsorbed by CaBC can be converted into inorganic phosphorus through biodegradation and mineralization, or recovered and directly used for agricultural fertilization, forming a closed-loop cycle of pollution-resource-agriculture (Chandrasekaran et al. 2024). However, the results of this study also demonstrate the significance of "customized" adsorption materials. Due to the differences in molecular structure, the mechanism of action of different organophosphorus is significantly different from that of CaBC, providing a design basis for the precise modification and scene adaptation of CaBC to match the structural requirements of pollutants, and promoting the upgrade of materials from general to specialized (Singh et al. 2023).

4 Conclusion

This study unveiled the leaching-control and sustained-release roles of calcium-modified biochar on different organic phosphorus. Manipulation experiments and theoretical calculations collectively confirmed that the interactions between OPs and CaBC were different. The adsorption of ATP occurred mainly through hydrogen bonding and electrostatic interactions, while that of the others took place through chemical precipitation, where calcium-based active sites played an important role. The specific adsorption and desorption rates of OPs could also be influenced by their molecular structures, including P groups and carbon chains. Therefore, our study proved the importance of considering component differences in controlling the leaching loss and improving the rational utilization of OPs. These differences persisted stably under different environmental conditions, including co-existing ions, ionic strength and pH. These findings would not only deepen the understanding of the coupling law of OPs' molecular structure-CaBC adsorption mechanism, but also lay a theoretical and technical foundation for precise design, scenario adaptation, and engineering application of biochar from general-purpose adsorption materials to targeted functional materials. Future research should focus on assessing the adsorption and desorption behaviors of CaBC for OPs in practical soil and waterbodies, thereby minimizing the environmental risks posed by P-class compounds in the natural environment. Moreover, customized optimization of CaBC should be carried out to maximize ecological benefits.

Supplementary Information

The online version contains supplementary material available at https://doi.org/10.1007/s42773-025-00562-z.

Supplementary material 1.

Author contributions

Ning Wang: Writing—original draft, Methodology, Investigation, Data curation, Formal analysis, Visualization, Conceptualization. Liangjie Tang: Writing—original draft, Investigation, Visualization. Xiaohui Zhang: Methodology, Investigation, Conceptualization. Dongtan Yao: Methodology, Investigation. Xiaolei Sun: Writing—review & editing, Methodology. Alain Mollier: Writing—review & editing, Methodology. Xiaolong Lin: Writing—review & editing, Methodology, Conceptualization. Xiaoqian Jiang: Writing—review & editing, Methodology, Conceptualization, Project administration, Funding acquisition.

Funding

This study was financially supported by the National Natural Science Foundation of China [Grant Number 42377323].

Data availability

The datasets used or analyzed during the current study are available from the corresponding author on reasonable request.

Declarations

Competing interests

The authors declare that they have no known competing financial interests or personal relationships that could have appeared to influence the work reported in this paper.

Author details

[1]School of Agriculture and Biotechnology, Sun Yat-Sen University, Guangzhou 510275, Guangdong, China. [2]State Key Laboratory of Forage Breeding-By-Design and Utilization, Key Laboratory of Vegetation and Environmental Change, Institute of Botany, Chinese Academy of Sciences, Beijing 100093, China. [3]University of Chinese Academy of Sciences, Beijing 100049, China. [4]ISPA, Bordeaux Sciences Agro, INRAE, 33140 Villenvce d'Ornon, France.

Received: 30 July 2025 Revised: 8 December 2025 Accepted: 15 December 2025
Published online: 11 February 2026

References

Agostinho AJ, de Souza Oliveira W, Anunciação DS, Santos JCC (2016) Simple and sensitive spectrophotometric method for phytic acid determination in grains. Food Anal Methods 9(7):2087–2096. https://doi.org/10.1007/s12161-015-0387-0

Andersson H, Bergström L, Djodjic F, Ulén B, Kirchmann H (2013) Topsoil and subsoil properties influence phosphorus leaching from four agricultural soils. J Environ Qual 42(2):455–463. https://doi.org/10.2134/jeq2012.0224

Benninghoven A (1994) Chemical analysis of inorganic and organic surfaces and thin films by static time-of-flight secondary ion mass spectrometry (TOF-SIMS). Angew Chem Int Ed Engl 33(10):1023–1043. https://doi.org/10.1002/anie.199410231

Cao H, Wu X, Syed-Hassan SSA, Zhang S, Mood SH, Milan YJ, Garcia-Perez M (2020) Characteristics and mechanisms of phosphorous adsorption by rape straw-derived biochar functionalized with calcium from eggshell. Bioresour Technol 318:124063. https://doi.org/10.1016/j.biortech.2020.124063

Chandrasekaran S, Jadhav S, Mari Selvam S, Krishnamoorthy N, Balasubramanian P (2024) Biochar-based materials for sustainable energy applications: a comprehensive review. J Environ Chem Eng 12(6):114553. https://doi.org/10.1016/j.jece.2024.114553

Chen A, Arai Y (2019) Functional group specific phytic acid adsorption at the ferrihydrite-water interface. Environ Sci Technol 53(14):8205–8215. https://doi.org/10.1021/acs.est.9b01511

Chen Y, Liu X, Chen J (2021) Steric hindrance effect on adsorption of xanthate on sphalerite surface: a DFT study. Miner Eng 165:106834. https://doi.org/10.1016/j.mineng.2021.106834

Chen A, Zhu L, Arai Y (2022) Solution NMR investigation of phytic acid adsorption mechanisms at the calcite-water interface. Sci Total Environ 840:156700. https://doi.org/10.1016/j.scitotenv.2022.156700

Chen S, Cai H, Du X, Wu P, Tao X, Zhou J, Dang Z, Lu G (2023) Adsorption behavior of hierarchical porous biochar from shrimp shell for tris(2-chloroethyl) phosphate (TCEP): sorption experiments and DFT calculations. Environ Res 219:115128. https://doi.org/10.1016/j.envres.2022.115128

Chen M, Liu Y, Pan J, Jiang Y, Zou X, Wang Y (2024) Low-cost Ca/Mg co-modified biochar for effective phosphorus recovery: adsorption mechanisms, resourceful utilization, and life cycle assessment. Chem Eng J 502:157993. https://doi.org/10.1016/j.cej.2024.157993

Dai Y, Wang W, Lu L, Yan L, Yu D (2020) Utilization of biochar for the removal of nitrogen and phosphorus. J Clean Prod 257:120573. https://doi.org/10.1016/j.jclepro.2020.120573

Du M, Zhang Y, Wang Z, Lv M, Xu Q, Chen Z, Wen Q, Li A (2022) La-doped activated carbon as high-efficiency phosphorus adsorbent: DFT exploration of the adsorption mechanism. Sep Purif Technol 298:121585. https://doi.org/10.1016/j.seppur.2022.121585

Fan S, Lu X, Li H, Du X, Huang X, Ma Y, Wang J, Tao X, Dang Z, Lu G (2022) Efficient removal of organophosphate esters by ligand functionalized MIL-101 (Fe): modulated adsorption and DFT calculations. Chemosphere 302:134881. https://doi.org/10.1016/j.chemosphere.2022.134881

Finšgar M (2023) Tandem GCIB-ToF-SIMS and GCIB-XPS analyses of the 2-mercaptobenzothiazole on brass. NPJ Mater Degrad 7(1):1. https://doi.org/10.1038/s41529-022-00317-2

Gerke J (2015) Phytate (Inositol Hexakisphosphate) in soil and phosphate acquisition from inositol phosphates by higher plants. A review. Plants (Basel) 4(2):253–266. https://doi.org/10.3390/plants4020253

Habiba U, Mutahir S, Khan MA, Humayun M, Refat MS, Munawar KS (2022) Effective removal of refractory pollutants through cinnamic acid-modified wheat husk biochar: experimental and DFT-based analysis. Catalysts 12(9):1063. https://doi.org/10.3390/catal12091063

Hashemzadeh F, Khoshmardan ME, Sanaei D, Ghalhari MR, Sharifan H, Inglezakis VJ, Arcibar-Orozco JA, Shaikh WA, Khan E, Biswas JK (2024) Adsorptive removal of anthracene from water by biochar derived amphiphilic carbon dots decorated with chitosan. Chemosphere 352:141248. https://doi.org/10.1016/j.chemosphere.2024.141248

Hilt F, Duday D, Gherardi N, Frache G, Bardon J, Choquet P (2013) Plasma deposition of an organophosphorus coating at atmospheric pressure. Plasma Process Polym 10:556. https://doi.org/10.1002/ppap.201300010

Huang Y, Hu H (2020) The interaction of perrhenate and acidic/basic oxygen-containing groups on biochar surface: A DFT study. Chem Eng J 381:122647. https://doi.org/10.1016/j.cej.2019.122647

Huang W, Li D, Liu Z, Tao Q, Zhu Y, Yang J, Zhang Y (2014) Kinetics, isotherm, thermodynamic, and adsorption mechanism studies of La(OH)3-modified exfoliated vermiculites as highly efficient phosphate adsorbents. Chem Eng J 236:191–201. https://doi.org/10.1016/j.cej.2013.09.077

Huang L, Yu Q, Liu W, Wang J, Guo W, Jia E, Zeng Q, Qin R, Zheng J, Hofmockel KS, Dong H, Jiang H, Zhu Z (2021) Molecular determination of organic adsorption sites on smectite during Fe redox processes using ToF-SIMS analysis. Environ Sci Technol 55(10):7123–7134. https://doi.org/10.1021/acs.est.0c08407

Huang X, Tie Y, Jiang J, Deng L, Che D (2023) Water washing of biomass and biochar. Sustain Energy Technol Assess 56:103066. https://doi.org/10.1016/j.seta.2023.103066

Huang P, Yang Z, Zhai K, Huang B, Zhou J, Sun X, Lin Y, Xu J, Pan C, Dong Y, Wang Y, Zhang Y, Lou Y, Huang H, Zhu Y, Zhang J (2025) Balancing *CHO/*CO intermediate flux via carbonyl-hydroxyl motif synergy enables high-selectivity ethanol electrosynthesis from dilute CO_2. J Am Chem Soc 147(25):22062–22071. https://doi.org/10.1021/jacs.5c05839

Khedulkar AP, Pandit B, Dang VD, Doong R-a (2023) Agricultural waste to real worth biochar as a sustainable material for supercapacitor. Sci Total Environ 869:161441. https://doi.org/10.1016/j.scitotenv.2023.161441

Koilraj P, Sasaki K (2017) Selective removal of phosphate using La-porous carbon composites from aqueous solutions: batch and column studies. Chem Eng J 317:1059–1068. https://doi.org/10.1016/j.cej.2017.02.075

Le Van K, Luong Thi TT (2014) Activated carbon derived from rice husk by NaOH activation and its application in supercapacitor. Prog Nat Sci Mater Int 24(3):191–198. https://doi.org/10.1016/j.pnsc.2014.05.012

Li S, Wang N, Chen S, Sun Y, Li P, Tan J, Jiang X (2023) Enhanced soil P immobilization and microbial biomass P by application of biochar modified with eggshell. J Environ Manage 345:118568. https://doi.org/10.1016/j.jenvman.2023.118568

Liang X, Guo N, Zhao Y, Xue F, Ren X, Yang Z, Yang Q (2022) Rapid effectual entrapment of pesticide pollutant by phosphorus-doped biochar: effects and response sequence of functional groups. J Mol Liq 365:120155. https://doi.org/10.1016/j.molliq.2022.120155

Liu X, Shen F, Qi X (2019) Adsorption recovery of phosphate from aqueous solution by CaO-biochar composites prepared from eggshell and rice straw. Sci Total Environ 666:694–702. https://doi.org/10.1016/j.scitotenv.2019.02.227

Ma J, Li J, Weng L, Ouyang X, Chen Y, Li Y (2023) Phosphorus-enhanced and calcium-retarded transport of ferrihydrite colloid: mechanism of electrostatic potential changes regulated via adsorption speciation. Environ Sci Technol 57(10):4219–4230. https://doi.org/10.1021/acs.est.2c09670

Manghi MC, Masiol M, Calzavara R, Graziano PL, Peruzzi E, Pavoni B (2021) The use of phosphonates in agriculture. Chemical, biological properties and legislative issues. Chemosphere 283:131187. https://doi.org/10.1016/j.chemosphere.2021.131187

McDowell RW, Worth W, Carrick S (2021) Evidence for the leaching of dissolved organic phosphorus to depth. Sci Total Environ 755:142392. https://doi.org/10.1016/j.scitotenv.2020.142392

Mei H, Laws TS, Terlier T, Verduzco R, Stein GE (2022) Characterization of polymeric surfaces and interfaces using time-of-flight secondary ion mass spectrometry. J Polym Sci 60(7):1174–1198. https://doi.org/10.1002/pol.20210282

Ni M, Ratner BD (2008) Differentiating calcium carbonate polymorphs by surface analysis techniques—an XPS and TOF-SIMS study. Surf Interface Anal 40(10):1356–1361. https://doi.org/10.1002/sia.2904

Ren C, Yu Z, Phillips BL, Wang H, Ji J, Pan B, Li W (2019) Molecular-scale investigation of fluoride sorption mechanism by nanosized hydroxyapatite using 19F solid-state NMR spectroscopy. J Colloid Interface Sci 557:357–366. https://doi.org/10.1016/j.jcis.2020.12.077

Rittmann BE, Mayer B, Westerhoff P, Edwards M (2011) Capturing the lost phosphorus. Chemosphere 84(6):846–853. https://doi.org/10.1016/j.chemosphere.2011.02.001

Ruttenberg KC, Sulak DJ (2011) Sorption and desorption of dissolved organic phosphorus onto iron (oxyhydr)oxides in seawater. Geochim Cosmochim Acta 75(15):4095–4112. https://doi.org/10.1016/j.gca.2010.10.033

Schindler DW, Carpenter SR, Chapra SC, Hecky RE, Orihel DM (2016) Reducing phosphorus to curb lake eutrophication is a success. Environ Sci Technol 50(17):8923–8929. https://doi.org/10.1021/acs.est.6b02204

Singh P, Rawat S, Jain N, Bhatnagar A, Bhattacharya P, Maiti A (2023) A review on biochar composites for soil remediation applications: comprehensive solution to contemporary challenges. J Environ Chem Eng 11(5):110635. https://doi.org/10.1016/j.jece.2023.110635

Sodhi RNS (2004) Time-of-flight secondary ion mass spectrometry (TOF-SIMS):—versatility in chemical and imaging surface analysis. Analyst 129(6):483–487. https://doi.org/10.1039/B402607C

Stockbridge RB, Wolfenden R (2009) The intrinsic reactivity of ATP and the catalytic proficiencies of kinases acting on glucose, N-acetylgalactosamine, and homoserine: a THERMODYNAMIC ANALYSIS*. J Biol Chem 284(34):22747–22757. https://doi.org/10.1074/jbc.M109.017806

Sun X, Bol R, Klumpp E, Li M (2022) Organic phosphorus leaching risk from agricultural soils across China. Chem Biol Technol Agric 9(1):35. https://doi.org/10.1186/s40538-022-00302-6

Tofan-Lazar J, Al-Abadleh HA (2012) Kinetic ATR-FTIR studies on phosphate adsorption on iron (oxyhydr)oxides in the absence and presence of surface arsenic: molecular-level insights into the ligand exchange mechanism. J Phys Chem A 116(41):10143–10149. https://doi.org/10.1021/jp308913j

Torres J, Veiga N, Savastano M, Kremer C, Bianchi A (2024) Interaction of phytate with cyclic polyamines. New J Chem 48(1):309–321. https://doi.org/10.1039/D3NJ04652D

Turner BL, Frossard E, Baldwin DS (2005) Organic phosphorus in the environment. CABI Publishing, Wallingford

Veiga N, Torres J, Macho I, Gómez K, González G, Kremer C (2014) Coordination, microprotonation equilibria and conformational changes of *myo*-inositol hexakisphosphate with pertinence to its biological function. Dalton Trans 43(43):16238–16251. https://doi.org/10.1039/C4DT01350F

Wan J, Li R, Feng X, Yang J, Ye Y, Jian S, Zhang X (2023) Insights into simultaneous adsorption of orthophosphate (PO_4^{3-}) and 1-hydroxyethane 1,1-diphosphonic acid (HEDP) by kaolin/lanthanum carbonate composites: experimental analysis and DFT calculations. Chem Eng J 476:146664. https://doi.org/10.1016/j.cej.2023.146664

Wang Z, Miao R, Ning P, He L, Guan Q (2021) From wastes to functions: a paper mill sludge-based calcium-containing porous biochar adsorbent for phosphorus removal. J Colloid Interface Sci 593:434–446. https://doi.org/10.1016/j.jcis.2021.02.118

Wang W, Tan J, Li S, Guan Y, Zhang X, Wang N, Liu J, Jiang X (2022) Transport, retention and release of phytate in soil with addition of Mg–Al layered double hydroxides. J Clean Prod 379:134774. https://doi.org/10.1016/j.jclepro.2022.134774

Wu Z, Deng W, Tang S, Ruiz-Hitzky E, Luo J, Wang X (2021) Pod-inspired MXene/porous carbon microspheres with ultrahigh adsorption capacity towards crystal violet. Chem Eng J 426:130776. https://doi.org/10.1016/j.cej.2021.130776

Xu S, Chen A, Arai Y (2021a) Solution ^{31}P NMR investigation of inositol hexakisphosphate surface complexes at the amorphous aluminum oxyhydroxide-water interface. Environ Sci Technol 55(21):14628–14638. https://doi.org/10.1021/acs.est.1c04421

Xu X, Luo P, Yang H, Pan S, Liu H, Hu X (2021b) Regulating the enzymatic activities of metal-ATP nanoparticles by metal doping and their application for H_2O_2 detection. Sens Actuators B Chem 335:129671. https://doi.org/10.1016/j.snb.2021.129671

Yan YP, Liu F Jr, Li W, Liu F, Feng XH, Sparks DL (2014a) Sorption and desorption characteristics of organic phosphates of different structures on aluminium (oxyhydr)oxides. Eur J Soil Sci 65(2):308–317. https://doi.org/10.1111/ejss.12119

Yan Y, Li W, Yang J, Zheng A, Liu F, Feng X, Sparks DL (2014b) Mechanism of Myo-inositol hexakisphosphate sorption on amorphous aluminum hydroxide: spectroscopic evidence for rapid surface precipitation. Environ Sci Technol 48(12):6735–6742. https://doi.org/10.1021/es500996p

Yan G, Gao Z, Zhao M, Yang W, Ding X (2020) A comprehensive exploration of mercury adsorption sites on the carbonaceous surface: a DFT study. Fuel 282:118781. https://doi.org/10.1016/j.fuel.2020.118781

Yang J, Zhang M, Wang H, Xue J, Lv Q, Pang G (2021) Efficient recovery of phosphate from aqueous solution using biochar derived from co-pyrolysis of sewage sludge with eggshell. J Environ Chem Eng 9(5):105354. https://doi.org/10.1016/j.jece.2021.105354

Yin Q, Liu M, Li Y, Li H, Wen Z (2021) Computational study of phosphate adsorption on Mg/Ca modified biochar structure in aqueous solution. Chemosphere 269:129374. https://doi.org/10.1016/j.chemosphere.2020.129374

Yin Y, Zhao Z, Wang G, Xu Y, Luan Y-n, Xie Y, Zhao J, Liu C (2024) Nanoconfinement of MgO in nitrogen pre-doped biochar for enhanced phosphate adsorption: performance and mechanism. Bioresour Technol 414:131613. https://doi.org/10.1016/j.biortech.2024.131613

Yuan M-y, Qiu S-k, Li M-m, Li Y, Wang J-X, Luo Y, Zhang K-q, Wang F (2023) Adsorption properties and mechanism research of phosphorus with different molecular structures from aqueous solutions by La-modified biochar. Environ Sci Pollut Res Int 30(6):14902–14915. https://doi.org/10.1007/s11356-022-23124-3

Zhang Y, Zhu C, Liu F, Yuan Y, Wu H, Li A (2019) Effects of ionic strength on removal of toxic pollutants from aqueous media with multifarious adsorbents: a review. Sci Total Environ 646:265–279. https://doi.org/10.1016/j.scitotenv.2018.07.279

Zhao Y, Xu M, Ren S, Yu J, Li T (2024) Ultra-high adsorption capacity of calcium-iron layered double hydroxides for HEDP removal through phase transition processes. Environ Sci Technol 58(43):19514–19522. https://doi.org/10.1021/acs.est.4c06464